

Optimal design of interpolation methods for time-delay interferometry

Martin Staab^{1,2}, Jean-Baptiste Bayle³, Olaf Hartwig⁴, Aurélien Hees¹, Marc Lilley¹, Graham Woan³, and Peter Wolf¹

¹ SYRTE, Observatoire de Paris, Université PSL, CNRS, Sorbonne Université, LNE, Paris, France

² Institute for Gravitational and Subatomic Physics (GRASP), Department of Physics, Utrecht University, Princetonplein 1, NL-3584 CC Utrecht, The Netherlands

³ University of Glasgow, Glasgow G12 8QQ, United Kingdom

⁴ Max Planck Institute for Gravitational Physics (Albert Einstein Institute), Hannover, Germany

E-mail: m.b.staab@uu.nl

Abstract. Time-delay interferometry (TDI) suppresses laser frequency noise by forming linear combinations of time-shifted interferometric measurements. The time-shift operation is implemented by interpolating discretely sampled data. To enable in-band laser noise reduction by eight to nine orders of magnitude, interpolation has to be performed with high accuracy. Interpolation can be understood as the convolution of an interpolation kernel with the data to be shifted. Optimizing the design of this interpolation kernel is the focus of this work. Previous research that studied constant time-shifts suggested Lagrange interpolation as the interpolation method for TDI. Its transfer function is maximally flat at DC and therefore performs well at low frequency. However, to be accurate at high frequencies, Lagrange interpolation requires a high number of coefficients. Furthermore, when applied in TDI we observed prominent time-domain features when a time-varying shift scanned over a pure integer sample shift. To limit this effect we identify an additional requirement for the interpolation kernel: when considering time-varying shifts the interpolation kernel must be sufficiently smooth to avoid unwanted time-domain transitions that produce glitch-like features in power spectral density estimates. The Lagrange interpolation kernel exhibits a discontinuous first derivative by construction, which is insufficient for the application to LISA or other space-based gravitational wave (GW) observatories. As a solution we propose a novel design method for interpolation kernels that respect a predefined requirement on in-band interpolation residuals and that possess continuous derivatives up to a prescribed order. Using this method we show that an interpolation kernel with 22 coefficients is sufficient to respect LISA's picometre-requirement and to allow for a continuous first derivative which suppresses the magnitude of the time-domain transition adequately. The reduction from 42 (Lagrange interpolation) to 22 coefficients enables us to save computational cost and increases robustness against artefacts in the data.

Submitted to: *Class. Quantum Grav.*

Keywords: LISA, gravitational-wave detection, laser-noise suppression, time-delay interferometry, interpolation.

1. Introduction

The Laser Interferometer Space Antenna (LISA) is an ESA-led space mission with a planned launch date in the mid-2030s to detect gravitational waves (GWs) in the frequency band from 0.1 mHz to 1 Hz [1], thereby filling the spectral gap between pulsar timing arrays and ground-based detectors like LIGO, Virgo and Kagra. The millihertz-regime is densely populated with a myriad of GW sources. The detection of those will shed new light on black hole formation history, test the strong-field gravity regime and trace GWs across cosmic ages [2] (for more information on the astrophysics with LISA see [3] and references therein).

LISA consists of three spacecraft separated by approximately 2.5 million kilometres forming a near-equilateral triangle. Each satellite carries two moveable optical sub-assemblies (MOSAs) that each host a laser source, an optical bench and a free-falling test-mass. Laser interferometry is employed to measure picometre-scale changes between those test-masses that serve as inertial reference points. The sensitivity of LISA is limited by spurious accelerations of the test masses at low frequencies, and by shot noise in the readout of the interferometric beatnotes at high frequency [1].

Instabilities of the central terahertz-frequency of the lasers necessitate ranging along at least two baselines. Comparison of the two ranging observables enables suppression of laser frequency noise. Ground-based detectors achieve this suppression by constructing Michelson interferometers with arms of equal length, so that the laser noise is cancelled upon recombination of the two beams. In space, test masses that represent the end-mirrors of the interferometers follow their individual orbital trajectories. Therefore, the triangle formed by the three LISA spacecraft is non-rigid, and is constantly flexing, so the light travel times along the six links differ by a few percent and fluctuate over the course of year with a typical rate of $3 \times 10^{-8} \text{ s s}^{-1}$ [4]. This renders the simple Michelson interferometer ineffective.

Furthermore, physically realizing round-trips to form equal-arm interferometers in space is impractical. Retro-reflection at the end-stations is unfeasible as laser beams diverge, and only a small fraction of the power (a few hundred picowatts [1]) is received by the distant satellite. The reflected beam would be reduced by the same factor on the return leg, down to immeasurable levels.

The solution is to rely on single-link measurements and construct virtual equal-arm interferometers in post-processing, on the ground. The time-delay interferometry (TDI) algorithm achieves this by time-shifting and linearly combining the single-link measurements. TDI enables realization of numerous interferometer topologies, e.g., Michelson-type or Sagnac-type [5, 6]. Due to LISA's unequal and flexing arms "higher-generations" of those topologies need to be considered, where the two virtual beams take multiple round-trips across the constellation to reduce the difference in travelled path length. In practice, the so-called second-generation variables, that suppress laser frequency noise up to first order in inter-spacecraft velocities and zeroth order in accelerations, are adequate for the LISA mission [7, 8].

The performance of TDI is limited by several technical laser noise residuals which enter at various stages in data processing [9]. On board the spacecraft, filters and decimators give rise to the flexing-filtering effect [10] and produce aliased laser noise. As shown in [11] the flexing-filtering effect can be mitigated, however any aliased laser noise remains in the data as an uncorrelated noise contribution. When performing TDI on the ground, ranging noise and interpolation errors couple to the final TDI variables. To reduce the effect of ranging noise, dedicated processing pipelines are being designed that combine information from different ranging sensors [12]. However, the impact of interpolation errors has not received much attention, and is therefore the subject of this paper.

TDI requires high-precision interpolation to effectively suppress laser frequency noise by up to nine orders of magnitude. Phase measurements taken on-board are sampled at a few Hertz and sent to the ground. To time-shift the data and construct TDI combinations in post-processing the time series are interpolated and re-evaluated on the shifted time grid [13]. The relative precision of the interpolation method must be of the order of 10^{-9} to respect the laser noise suppression ratio. Lagrange interpolation was identified to outperform other methods (windowed sinc) using the fewest number of interpolation coefficients [13]. Therefore, efficient algorithms to calculate those were developed and traditionally used in data processing pipelines for space-based GW observatories [14].

However, in this paper, we will show that Lagrange interpolation is suboptimal for two reasons. First, when considering realistic LISA data involving time-dependent time-shifts, the interpolation error becomes non-stationary. This produces prominent time-domain features which are connected to sudden changes in the interpolation coefficients. For Lagrange interpolation, this happens when the time-shift passes through an integer number of sampling periods as the interpolation coefficients adjust in a non-smooth fashion. This property was missed in previous studies, as only constant time-shifts were considered. Second, we find that Lagrange interpolation uses a relatively large number of coefficients which requires more computational resources and increases the amount of invalid samples at the boundaries of the time series.

To remedy both shortcomings, we will present a novel interpolation method. It allows for specifying the smoothness of the kernel function, i.e. the function from which the interpolation coefficients are drawn. We find that a continuous first derivative suffices to suppress the time-domain feature to adequate levels. Furthermore, we describe an optimization routine to minimize the number of interpolation coefficients while retaining sufficient laser noise suppression over the entire LISA band.

The paper is organized as follows. In section 2 we introduce the basic concept of TDI and explain the coupling of interpolation errors. Then, in section 3 we develop a general framework to describe interpolation as a convolution of a kernel function and the data. We derive the kernel function for Lagrange interpolation in section 4 and present its shortcomings. As a solution, in section 5 we introduce a novel class of kernel functions dubbed cosine-sum kernels. Finally, in section 6 we validate our findings for

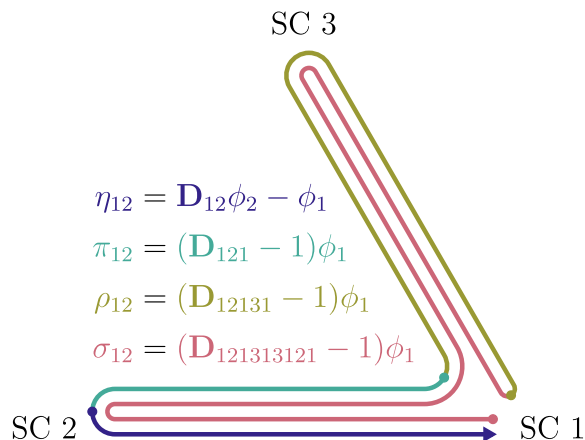


Figure 1. Illustration of the working principle of TDI. Increasingly longer virtual photon paths are constructed by hierarchically building up the intermediary variables π , ρ and σ as defined in equations 4, 7 and 8. In the final step the two round-trip variables σ_{12} and σ_{13} are subtracted to form the second-generation Michelson variable X_2 . The two synthesized counter-propagating photon paths have almost identical length, hence, laser noise is greatly suppressed. Adopted from [9].

both interpolation methods by running numerical simulations, and conclude in section 7.

2. Interpolation errors in TDI

LISA does not physically realize equal-arm interferometers in space. Instead, it relies on the so-called split-interferometry setup which employs three interferometers on each of the six optical benches: the inter-spacecraft, the reference and the test-mass interferometer. The inter-spacecraft interferometer mixes light from the distant laser that has travelled to the local optical bench, thereby integrating the GW strain along the line-of-sight. In the reference interferometer, the adjacent laser is compared to the local laser via the backlink fibre. Finally, the test-mass interferometer is almost identical to the reference interferometer with the difference that the adjacent light is bounced off the test mass, which serves as an inertial reference for the ranging measurement. [1]

The aforementioned interferometers are then combined to form the six single-link measurements η_{ij} [6]. First, the inter-spacecraft and test-mass interferometers are combined to compensate for the longitudinal relative motion between the optical bench and the test-mass. Then, the reference interferometers are brought in to reduce the number of lasers to one per spacecraft. The single-link measurements, in terms of laser phases ϕ_i , are therefore given by

$$\eta_{ij}(t) = \mathbf{D}_{ij}\phi_j(t) - \phi_i(t). \quad (1)$$

Here, i denotes the local and j the distant spacecraft index. The time-delay operator \mathbf{D}_{ij} models the propagation of the distant laser phase ϕ_j to the local spacecraft by delaying it by the pseudo-range $d_{ij}(t)$ expressed as time. We formally define the general delay

operation as

$$\mathbf{D}x(t) = x(t - d(t)). \quad (2)$$

In LISA, the time-delay $d(t)$ contains the "macroscopic" light travel time of about eight seconds, the result of desynchronization between time reference frames (relativistic effects and clock imperfections) and the path-length variations due to GWs. Dedicated ranging sensors are implemented in LISA to measure all six delays d_{ij} independently of the carrier-carrier beatnote.

The ultimate goal of TDI is to suppress laser noise by constructing virtual equal-arm interferometers; in our example, a simple Michelson interferometer. In the first step we cancel the distant laser from η_{ij} by constructing round-trip interferometers as illustrated in figure 1. This is achieved by adding a delayed version of the distant readout η_{ji} as

$$\pi_{ij} = \eta_{ij} + \mathcal{D}_{ij}\eta_{ji} \quad (3)$$

$$= (\mathbf{D}_{iji} - 1)\phi_i + \underbrace{(\mathcal{D}_{ij} - \mathbf{D}_{ij})}_{\Delta_{ij}}\eta_{ji}. \quad (4)$$

Here, we introduce the so-called "post-processing" delay \mathcal{D} that is applied on the ground. As the raw interferometric measurements are discretely sampled at a few hertz, we rely on interpolation to apply arbitrary time-shifts in TDI. Therefore, the post-processing delay operator \mathcal{D} represents only an approximation of the true delay \mathbf{D} defined in (2). Any deviation of the post-processing from the true delay operator is described by the interpolation error Δ_{ij} . In reality, the post-processing delay operator is also impacted by other imperfection, e.g., ranging biases [9]. However, here we only focus on the residual laser noise in the final TDI variables resulting from interpolation errors.

In (4) we introduce the short-hand notation for nested delays. In general, we define the contracted delay operator

$$\mathbf{D}_{i_1 \dots i_N} \equiv \mathbf{D}_{i_1 i_2} \dots \mathbf{D}_{i_{N-1} i_N}, \quad (5)$$

where the associated nested time-delay $d_{i_1 \dots i_N}(t)$ can be calculated recursively. The equivalence in (5), however, does not hold for the post-processing delay operator \mathcal{D} as each application introduces additional interpolation errors. Consequently, the results of $\mathcal{D}_{i_1 \dots i_N}x(t)$ and $\mathcal{D}_{i_1 i_2} \dots \mathcal{D}_{i_{N-1} i_N}x(t)$ generally differ.

Now, we take the difference of two adjacent round-trip measurements and yield the simple Michelson interferometer,

$$X_0 = \pi_{13} - \pi_{12} = (\mathbf{D}_{131} - \mathbf{D}_{121})\phi_1 + (\Delta_{13}\eta_{31} + \Delta_{12}\eta_{21}). \quad (6)$$

In the equal-arm assumption, laser noise from the first term cancels, leaving only laser noise residuals due to interpolation errors from the second term. In a realistic LISA setup inter-spacecraft delays are unequal and time-varying. Therefore, the second-generation

Michelson variable X_2 is required to achieve nearly equal arms and suppress laser noise effectively (see figure 1 and also [5]). Let us define the (intermediary) variables as in [9]

$$\rho_{ij} = \pi_{ij} + \mathcal{D}_{iji}\pi_{ik}, \quad (7)$$

$$\sigma_{ij} = \rho_{ij} + \mathcal{D}_{ijiki}\rho_{ik}, \quad (8)$$

$$X_2 = \sigma_{13} - \sigma_{12} \approx [[\mathbf{D}_{131}, \mathbf{D}_{121}], \mathbf{D}_{12131}]\phi_1 + \delta X_2^{\mathcal{D}}. \quad (9)$$

Here, the delay operator difference in the last line is expressed as nested commutators to emphasize that the fundamental laser noise residual is limited by contributions quadratic in velocities \dot{d}_{iji} and linear in accelerations \ddot{d}_{iji} . The interpolation residual $\delta X_2^{\mathcal{D}}$ collects terms from the various intermediate variables[‡] π_{ij} , ρ_{ij} and σ_{ij} [9]. Here, we make the particular choice of applying the nested post-processing delays \mathcal{D}_{iji} ($\neq \mathcal{D}_{ij}\mathcal{D}_{ji}$) and \mathcal{D}_{ijiki} ($\neq \mathcal{D}_{ij}\mathcal{D}_{ji}\mathcal{D}_{ik}\mathcal{D}_{ki}$) for the sake of computational efficiency. The implications of this factorization are further discussed in [9]. Moreover, we neglect second-order couplings in $\delta X_2^{\mathcal{D}}$, i.e. couplings of interpolation errors to interpolation residuals, as the latter is already small compared to the laser noise content.

3. The interpolation kernel

Let us now turn to the actual implementation of the post-processing delay \mathcal{D} for TDI. The operation is performed in two steps, summarized in figure 2. First, the discrete-time samples $x(nT_s)$ (illustrated as blue dots) of the original time series are interpolated. Here, T_s denotes the sampling interval between samples. This is achieved by taking the weighted sum of samples close to the time of interest achieving locality of the operation. The weights are drawn from the so-called interpolation kernel which is shown in black. Formally we define the continuous-time interpolated signal as

$$\bar{x}(t) = \sum_{m=-\infty}^{\infty} x(mT_s) \cdot k(t - mT_s). \quad (10)$$

The choice of kernel function determines the quality of the interpolation. For perfect band-limited interpolation one would need to set $k(\tau) = \text{sinc}(f_s\tau) = \frac{\sin(\pi f_s\tau)}{\pi f_s\tau}$ which yields the Whittaker-Shannon interpolation formula [15]. The critical downside of this approach is that the sinc-kernel is infinitely wide, so the sum in (10) runs over an infinite number of elements. To make the computation feasible, we only consider kernels of finite width T . Furthermore, we limit ourselves to the class of real and even functions, i.e. symmetric in τ and possessing a real and even Fourier transform, which becomes important later.

In the next step, we apply the delay d to the interpolated time series $\bar{x}(t)$ and

[‡] The index k appearing in equations 7, 8 and 9 denotes the remaining spacecraft index that is different from i and j .

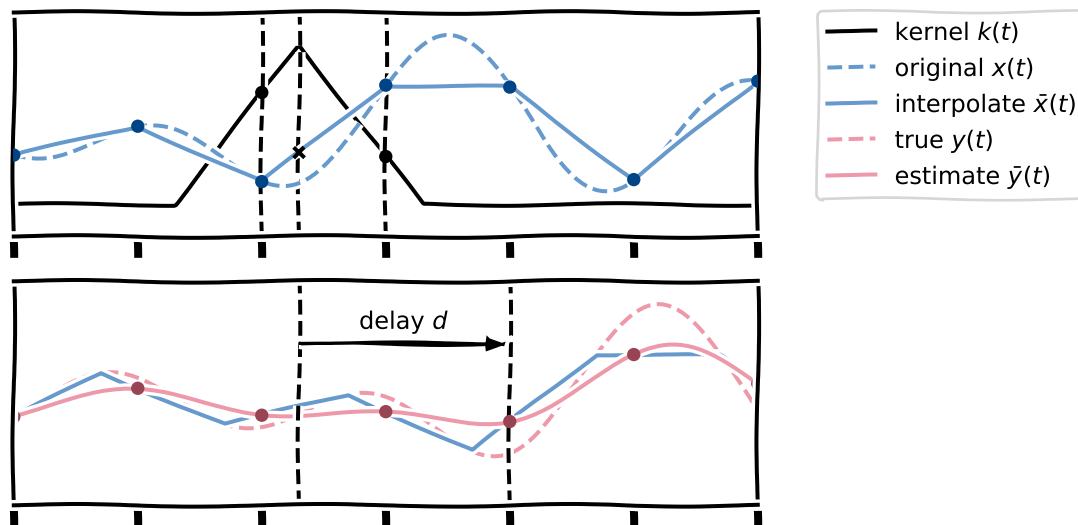


Figure 2. Illustration of the post-processing delay operation. In the upper panel, the solid blue line depicts a simple linear interpolation between discrete samples (blue dots) of the continuous band-limited signal $x(t)$ (dashed blue line). The black line shows the corresponding triangular interpolation kernel. To interpolate at a given time (black cross) the neighbouring samples are weighted by the corresponding readings of the kernel function (black dots). In the lower panel we plot the time-delayed interpolated signal in blue, its sampled version (the result of (13)) as red dots and its continuous-time band-limited equivalent (red line). In dashed red we overlay the true delayed signal. We observe an amplitude and phase error between the post-processing delay operation and the true delay operation.

sample it on the original time grid. Formally, This translates to

$$\bar{y}(nT_s) = \bar{x}(t - d)|_{t=nT_s}, \quad (11)$$

$$= \sum_{m=-\infty}^{\infty} x(mT_s) \cdot k((n - m)T_s - d), \quad (12)$$

$$= \sum_{m=-\infty}^{\infty} x((n - m)T_s) \cdot k(mT_s - d), \quad (13)$$

which yields the delayed time series depicted as red dots in figure 2. In the last line we performed the substitution $m \rightarrow n - m$ to identify the delay operation as a discrete convolution of the original time series $x(nT_s)$ and the sampled delayed kernel function $k(nT_s - d)$.

In the following, we reformulate the post-processing delay operation in continuous time by using the Whittaker-Shannon interpolation formula. This enables us to identify the transfer function of the operation, which can be used to assess its performance. The Whittaker-Shannon formula states that a time series $x(t)$ that is band-limited up to

some frequency $f_s/2$ can be represented by discrete samples as

$$x(t) = \sum_{n=-\infty}^{\infty} x(nT_s) \cdot \text{sinc}(f_s t - n). \quad (14)$$

We use this formula to identify the continuous-time representation of $\bar{y}(mT_s)$ and find that the post-processing delay operation can indeed be represented as a linear time-invariant (LTI) system for constant time-shifts

$$\bar{y}(t) = \sum_{n=-\infty}^{\infty} \bar{y}(nT_s) \cdot \text{sinc}(f_s t - n), \quad (15)$$

$$= \sum_{m,n=-\infty}^{\infty} x((n-m)T_s) \cdot k(mT_s - d) \cdot \text{sinc}(f_s t - n), \quad (16)$$

$$= \int_{-\infty}^{\infty} \underbrace{k(\tau - d) \sum_{m=-\infty}^{\infty} \delta(\tau - mT_s)}_{h(\tau;d)} \cdot x(t - \tau) d\tau, \quad (17)$$

where we have introduced the integral over the Dirac-delta function to identify $h(\tau; d)$ as the impulse response of the operation given the delay d . Taking the Fourier transform of the latter lets us derive the transfer function $\tilde{h}(f; d)$ as

$$\tilde{h}(f; d) = \sum_{m=-\infty}^{\infty} k(mT_s - d) \cdot e^{-2\pi i f m T_s}, \quad (18)$$

$$= f_s \sum_{m=-\infty}^{\infty} \tilde{k}(f - m f_s) \cdot e^{-2\pi i (f - m f_s) d}. \quad (19)$$

Here, we list two equivalent forms[§]: The first one is convenient for numerical calculations as the sum can be simplified to only run over a finite number of indices when considering kernels of finite width. Furthermore, the kernel function $k(t)$ is readily available to draw the required samples $k(mT_s - d)$. The second representation can be understood as the spectral folding (similar to aliasing) of the Fourier transform of the kernel multiplied with the transfer function of the delay operation, i.e. the complex exponential $e^{-2\pi i f d}$. We note that any components of $\tilde{k}(f)$ residing outside of the band-limit (i.e. for frequencies $|f| > f_s/2$) give rise to a phase error in the post-processing delay operation.

3.1. Interpolation error

Let us study the amplitude and phase error of the post-processing constant delay operation more systematically. We define the interpolation error as the deviation of

[§] The first expression is obtained by inserting $h(\tau; d)$ into the definition of the Fourier transform while the second line is obtained by using the fact that $h(\tau; d)$ is the convolution of $k(t)$ with a Dirac comb whose Fourier transform is also a Dirac comb.

the post-processing delay operation from the true delay operation

$$\bar{y}(t) - y(t) = \underbrace{\mathcal{D}x(t)}_{(h*x)(t)} - \underbrace{\mathbf{D}x(t)}_{x(t-d)}. \quad (20)$$

Let $x(t)$ be a band-limited random process with power spectral density (PSD) $S_x(f)$. Then, we can characterize the interpolation error by calculating its PSD. As the operation $\Delta = \mathcal{D} - \mathbf{D}$ is a LTI system itself we can readily write down the result which is given as the product of the magnitude squared of its transfer function and the original PSD (see e.g. [9])

$$S_{\Delta}(f) = \underbrace{|\tilde{h}(f; d) - e^{-2\pi i f d}|^2}_{\Delta} \cdot S_x(f), \quad (21)$$

$$\leq \left(\left| f_s \tilde{k}(f) - 1 \right| + \sum_{m \neq 0} \left| f_s \tilde{k}(f - m f_s) \right| \right)^2 \cdot S_x(f). \quad (22)$$

In the second line we have additionally derived an upper bound for the result which is independent of the delay d . Here, we have used the triangle inequality to move the norm $|\cdot|^2$ under the sum. From this expression we can derive the condition for the ideal interpolation kernel. For the upper limit to vanish, the Fourier transform of the ideal interpolation kernel must be equal to $\frac{1}{f_s}$ up to the Nyquist frequency and equal to zero past it; which describes the scaled rectangular function that is the Fourier transform of the sinc-kernel. As discussed previously, the sinc-kernel is not an appropriate choice as it has infinite width. Therefore, in sections 4 and 5 we discuss two possible interpolation methods with kernel functions of finite width; Lagrange interpolation and cosine-sum kernels.

3.2. Interpolation glitch

Until now, we have only considered constant delays. However, in LISA inter-spacecraft distances are time-dependent with maximum rates of $3 \times 10^{-8} \text{ s s}^{-1}$ [4]. Therefore, TDI also has to apply time-varying post-processing delay operations to suppress laser frequency noise effectively [16]. As a result the interpolation error derived in (20) becomes non-stationary and can produce prominent glitch-like time-domain transitions (see figure 8 as an example) if the interpolation kernel is not carefully designed.

The overall smoothness of the kernel function $k(t)$ determines the amplitude and the time of occurrence of the interpolation glitch. Let us take the example of linear interpolation which is presented in figure 2. The kernel for linear interpolation is given by the triangular function whose first derivative is discontinuous at $t \in \{-T_s, 0, T_s\}$. Those discontinuities are inherited by the interpolated function $\bar{x}(t)$ at $t = nT_s$ where $n \in \mathbb{Z}$. Therefore, when the delay becomes an integer multiple of the sampling time T_s the delayed signal $\bar{y}(nT_s)$ scans over such a discontinuity. As a result, the interpolation error changes abruptly and appears to be incoherent before and after the critical time.

We can estimate the impact of this effect by studying the spectral content of a finite stretch of the delayed time-series $\bar{y}(t)$ around a critical point t_0 which corresponds to a critical delay $d_0 = d(t_0)$ where some derivative $k^{(q)}(mT_s - d_0)$ in (13) is discontinuous (in the case of linear interpolation it is the first derivative). We assume that the delay $d(t)$ changes slowly with time, hence, we can approximate it as a linear function in the vicinity of t_0 ,

$$d(t) = d_0 + \dot{d} \cdot (t - t_0). \quad (23)$$

Then, we turn (13) to the continuous-time case by replacing $nT_s \rightarrow t$, set $d = d(t)$ and Taylor-expand in the small quantity $\dot{d}(t - t_0)$. We recognize that we can decompose $\bar{y}(t)$ into several components

$$\bar{y}(t) = \bar{y}_{\text{const}}(t) + \bar{y}_{\text{cont}}(t) + \bar{y}_{\text{disc}}(t), \quad (24)$$

where,

$$y_{\text{const}}(t) = \sum_{m=-\infty}^{\infty} x(t - mT_s) k(mT_s - d_0), \quad (25)$$

$$\bar{y}_{\text{cont}}(t) = \sum_{m=-\infty}^{\infty} \sum_{q=1}^{\infty} x(t - mT_s) \bar{k}^{(q)}(mT_s - d_0) \frac{(-\dot{d} \cdot (t - t_0))^q}{q!}, \quad (26)$$

$$\bar{y}_{\text{disc}}(t) = -\text{sgn}(t - t_0) \sum_{m=-\infty}^{\infty} \sum_{q=1}^{\infty} x(t - mT_s) \Delta k^{(q)}(mT_s - d_0) \frac{(-\dot{d} \cdot (t - t_0))^q}{q!}. \quad (27)$$

The first component $y_{\text{const}}(t)$ represents the zeroth order term in the expansion and is equivalent to a constant delay (cf. (13) with $d = d_0$). The remaining constituents $\bar{y}_{\text{cont}}(t)$ and $\bar{y}_{\text{disc}}(t)$ are small (higher order in \dot{d}) corrections that capture the time-varying character of the delay. Here, the former capture the smooth (or continuous) components in time and the latter the discontinuous ones. Here, we recognize the sgn -function, which is defined as the sign of its argument (the exception is $\text{sgn}(0) = 0$). Furthermore, the functions $\bar{k}^{(q)}(\tau)$ and $\Delta k^{(q)}(\tau)$ characterize the offset and the magnitude of the discontinuities in the q -th derivative of the kernel function. They are formally defined as,

$$\bar{k}^{(q)}(\tau) = \frac{k_+^{(q)}(\tau) + k_-^{(q)}(\tau)}{2}, \quad (28)$$

$$\Delta k^{(q)}(\tau) = \frac{k_+^{(q)}(\tau) - k_-^{(q)}(\tau)}{2}, \quad (29)$$

where $k_{\pm}^{(q)}(\tau) = \lim_{\epsilon \rightarrow 0^+} k^{(q)}(\tau \pm \epsilon)$ are the derivatives approached from the right and left.

|| To turn back to the discrete-time case we can simply sample this expression at $t = nT_s$ again which will cause aliasing in the spectral estimate. We do not include this effect in the modelling as it is subdominant.

Let us now study the contribution of each component in (24) to an estimate of the PSD; the periodogram. For a general time-series $z(t)$ of length T , the periodogram is defined as $T|Z(f)|^2$. Here, $Z(f)$ is the windowed Fourier transform of $z(t)$ (centred on t_0), formally given as

$$Z(f) = \frac{1}{T} \int_{-T/2}^{T/2} w(t) \cdot z(t + t_0) \cdot e^{-2\pi i f t} dt. \quad (30)$$

The window function $w(t)$ must be chosen appropriately to limit the naturally occurring spectral leakage. Throughout this study we use a Kaiser window [17] with $\beta = 30$ that possesses a sidelobe attenuation of 280 dB. As a result of the stochastic nature of laser noise, the periodogram $T|Z(f)|^2$ is a random variable itself. Therefore, to make predictions, we work with its expectation value

$$\mathcal{S}_z(f) \equiv \mathbb{E} \{ T |Z(f)|^2 \}, \quad (31)$$

$$\sim \frac{1}{T} [|\tilde{w}(f')|^2 * S_z(f')] (f), \quad (32)$$

denoted with a calligraphic \mathcal{S} to distinguish it from the true power spectral density $S_z(f)$. If $z(t)$ is a stationary random process the second line holds where we make use of the fact that the Fourier transform of the auto-correlation function $R_z(\tau) = \mathbb{E}\{z(t) \cdot z(t+\tau)\}$ is equal to $S_z(f)$. Here, we can observe natural spectral leakage as the true PSD $S_z(f)$ being viewed through the spectral window $|\tilde{w}(f')|^2$. This is the case for the constant-delay component $y_{\text{const}}(t)$ whose (expected) periodogram yields

$$\mathcal{S}_{\bar{y}_{\text{const}}}(f) = \frac{1}{T} \left[|\tilde{w}(f')|^2 * \left(\left| \tilde{h}(f; d_0) \right|^2 \cdot S_x(f) \right) \right] (f), \quad (33)$$

and thus is equivalent to $|\tilde{h}(f; d_0)|^2 \cdot S_x(f)$ up to natural spectral leakage (similar to (21)).

On the contrary, the components $\bar{y}_{\text{cont}}(t)$ and $\bar{y}_{\text{disc}}(t)$ in (24) are non-stationary. Therefore, the equality in (32) does not hold any more. We reevaluate (31) for the discontinuous component $\bar{y}_{\text{disc}}(t)$ as the sgn-function gives rise to additional spectral leakage. We find

$$\mathcal{S}_{\bar{y}_{\text{disc}}}(f) \approx \frac{d^{2\hat{q}}}{T} \left[|\tilde{v}_{\hat{q}}(f')|^2 * \left(\left| \Delta \tilde{h}_{\hat{q}}(f') \right|^2 \cdot S_x(f') \right) \right] (f), \quad (34)$$

where $\tilde{v}_{\hat{q}}(f)$ denotes the Fourier transform of the modified window function defined as

$$v_{\hat{q}}(t) = w(t) \cdot \text{sgn}(t) \cdot \frac{t^{\hat{q}}}{\hat{q}!}, \quad (35)$$

and $|\Delta \tilde{h}_{\hat{q}}(f)|^2$ is a transfer-function-like factor given as

$$|\Delta \tilde{h}_{\hat{q}}(f)|^2 = \left| \sum_m \Delta k^{(\hat{q})}(mT_s - d_0) \cdot e^{-2\pi i f m T_s} \right|^2. \quad (36)$$

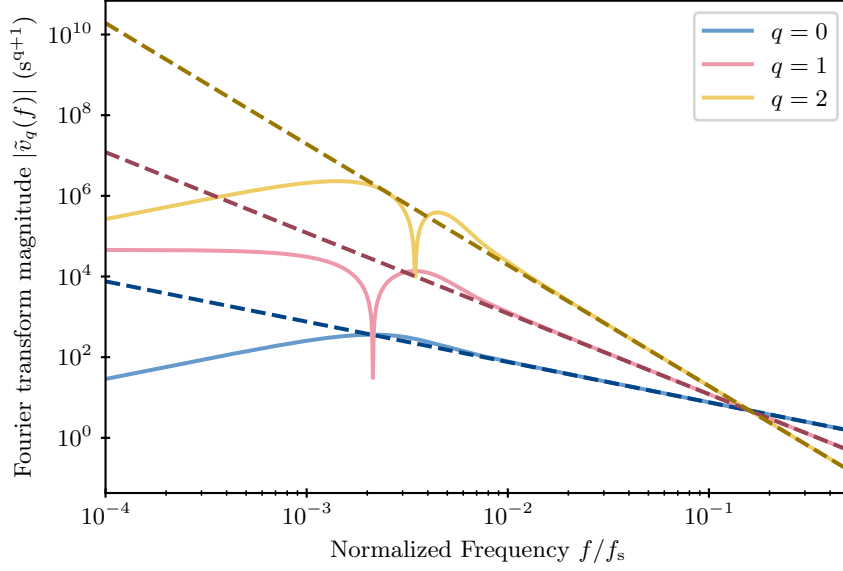


Figure 3. One-sided representation of the modified spectral window magnitude $|\tilde{v}_q(f)|$ assuming a Kaiser window with β of 30 and an observation time T of 10 000 s. Results for $q = 0$ (blue), $q = 1$ (red) and $q = 2$ (yellow) are shown. The dashed lines show the limit $f \gg \frac{1}{T}$.

In (34) we limit ourselves to only the leading order contribution in \dot{d} , i.e., the degree $q = \hat{q}$ of the lowest-order derivative that is discontinuous. For $q < \hat{q}$ the derivatives $k^{(q)}(\tau)$ are actually continuous and hence $|\Delta\tilde{h}_q(f)|^2$ vanishes. Contributions from higher degrees $q > \hat{q}$ are higher order in \dot{d} and are therefore negligible.

The derived model in (34) is similar to (33), however, the original spectral window $\tilde{w}(f)$ is exchanged by the modified spectral window $\tilde{v}_{\hat{q}}(f)$ and the PSD of the original time series is adjusted by the transfer function $|\Delta\tilde{h}_{\hat{q}}(f)|^2$. We plot the modified window $\tilde{v}_q(f)$ in figure 3 for different degrees q . We observe weak attenuation at frequencies larger than the frequency resolution $\Delta f = \frac{1}{T}$ where the spectral windows take the form $|\tilde{v}_q(f)| \rightarrow \frac{2|w(0)|}{(2\pi f)^{q+1}}$ and thus only decay as $f^{-(q+1)}$.

In summary, the magnitude of additional leakage due to an interpolation glitch is strongly dependent on the smoothness of the interpolation kernel. The more continuous derivatives the kernel function has (up to some degree \hat{q}) the weaker the impact of additional leakage and the stronger the suppression due to the factor $\dot{d}^{2\hat{q}}$. Moreover, the magnitude of the discontinuity $\Delta k^{(q)}(\tau)$ plays a role. Through out this study we choose parameters representative of the LISA mission. We assume a maximum delay derivative of $\dot{d} = 10^{-7}$ which is a typical value for the round-trip delay in LISA (applied in the σ variable, see (8)) and a duration of $T = 10\,000$ s to enable spectral resolution at the low-frequency end of the LISA band, i.e., 0.1 mHz. We will discuss the expected levels of additional leakage for Lagrange interpolation and the cosine-sum kernel in the forthcoming sections.

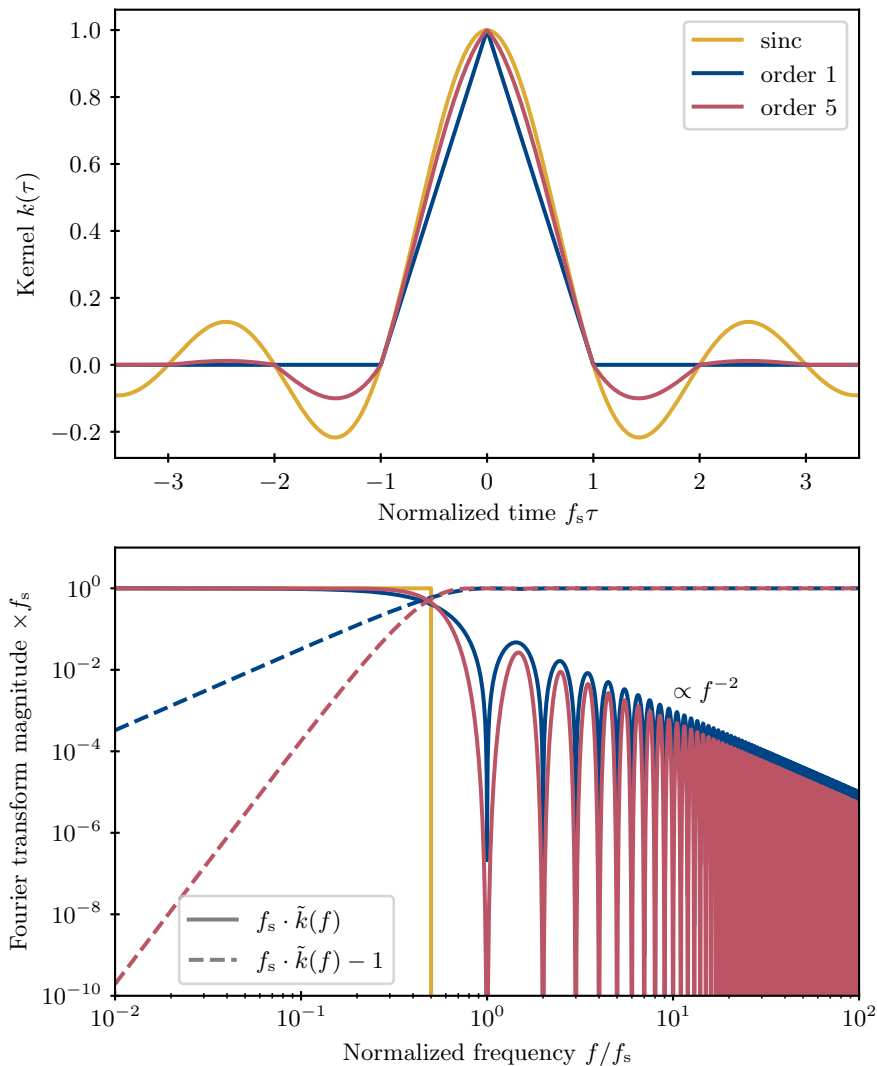


Figure 4. Lagrange kernel functions (upper panel) and their corresponding Fourier transform (lower panel) for orders 1 (blue) and 5 (red). For comparison, we also plot the result for the sinc-kernel which is the limit for Lagrange kernels of increasing order. In the lower panel we additionally show the difference of $f_s \cdot |\tilde{k}(f)|$ from unity as dashed lines.

4. Lagrange Interpolation

The most common interpolation method for TDI in LISA is Lagrange interpolation [13]. It provides excellent low-frequency performance, as its response in the Frequency domain is maximally flat at DC. Lagrange interpolation is based on the Lagrange polynomial which fits N data points using an $(N - 1)$ -th degree polynomial. Assuming that data points are equally spaced by the sampling time T_s and we always choose the data points such that the resulting polynomial is evaluated close to the barycentre of the points, we arrive at the following piece-wise definition of the kernel function $k(\tau)$. For

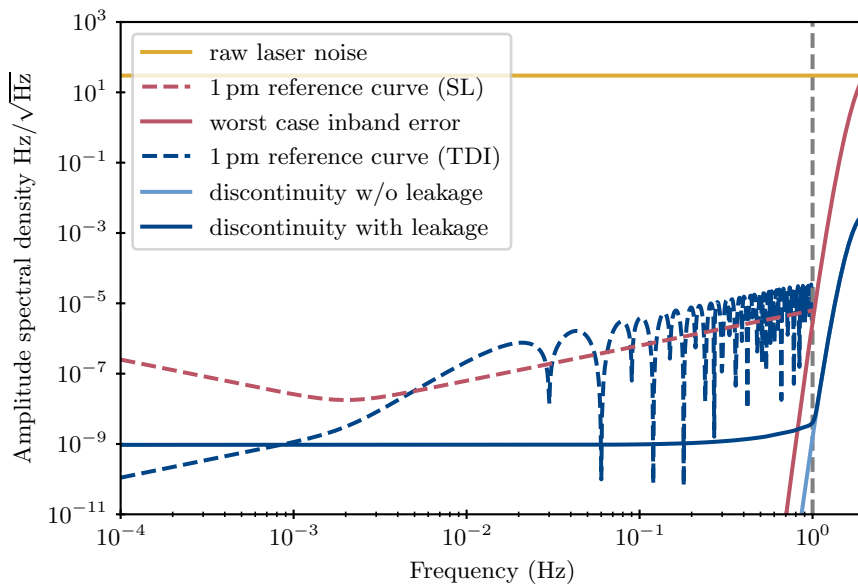


Figure 5. Amplitude spectral densities (ASDs) of interpolation errors for Lagrange interpolation order 41 operating on laser noise (in yellow) with an ASD of $30 \text{ Hz}/\sqrt{\text{Hz}}$. The light red line shows the worst case interpolation error (see (22)) which stays below the single link (SL) 1 pm reference curve (dashed dark red) in band. An estimate of the ASD caused by the discontinuity of $k'(\tau)$ (i.e. $q = 1$) is shown in blue with (dashed-dotted line) and without leakage (solid line). Here, we assume a duration of $T = 10000 \text{ s}$, a delay derivative of $\dot{d} = 10^{-7}$ and a Kaiser window with $\beta = 30$. We note that in-band frequencies are dominated by leakage, which violates the 1 pm reference curve after TDI [9] (dashed blue).

$m = 0, \dots, N/2 - 1$ we define

$$k_m(\tau) = \prod_{\substack{n=-N/2 \\ n \neq m}}^{N/2-1} 1 + \frac{|f_s \tau|}{n - m} \quad \text{valid for } m \leq |f_s \tau| < m + 1. \quad (37)$$

For $|f_s \tau| \geq N/2$ the kernel function is set to zero.

In the upper panel of figure 4 we plot the kernel function $k(\tau)$ for polynomial order 1 ($N = 2$) in blue and 5 ($N = 6$) in red. The piece-wise polynomial definition becomes apparent as $k(\tau)$ exhibits non-smooth transitions at integer multiples of the sampling time T_s . For increasing order the kernel function converges to the sinc-function (in yellow), which represent ideal band-limited interpolation.

To assess the in-band performance of Lagrange interpolation we derive the Fourier transform of the kernel $\tilde{k}(f)$ which is of the form

$$\tilde{k}(f) = \frac{1}{f_s} \cdot P((\pi f/f_s)^2) \cdot \text{sinc}^N(f/f_s), \quad (38)$$

where $P(x)$ is a polynomial of degree $N/2 - 1$. In the lower panel of figure 4 we plot $\tilde{k}(f)$ for orders 1 and 5. Here, we can clearly observe the maximal-flatness property of the

Lagrange kernel as at low frequencies the difference of $f_s \cdot \tilde{k}(f)$ from unity follows a power law of order N (therefore, derivatives of $\tilde{k}(f)$ evaluated at $f = 0$ Hz up to order $N-1$ are vanishing). At frequencies past the Nyquist frequency, regardless of the interpolation order, the magnitude of $\tilde{k}(f)$ decays with f^{-2} as a result of the discontinuous first derivative of the kernel function. At first sight, this slow decay seems problematic as it produces large aliased contributions when evaluating the in-band interpolation error (see (22)). However, since $\tilde{k}(f)$ quickly drops to zero at integer multiples of f_s (due to the sinc-function in (38)) which are aliased to dc the impact is greatly reduced and most of the high-frequency content of $\tilde{k}(f)$ is folded to frequencies close to the Nyquist frequency.

To reduce the impact of interpolation errors below 1 Hz in LISA we require a minimum order of 41 [9]. We illustrate this in figure 5 where we plot the worst case in-band interpolation error (red) for any constant delay for the usual level of white laser frequency noise with a level of $30 \text{ Hz}/\sqrt{\text{Hz}}$ (yellow). For in-band frequencies, the interpolation error is strictly below the single-link 1 pm reference curve (dashed red).

Problems arise when considering a time-varying delay. As discussed in the previous section, discontinuities in derivatives of the kernel function $k^{(q)}(\tau)$ give rise to prominent time-domain features that introduce additional power in ASD estimates. Taking a closer look at (37) reveals that odd derivatives of $k(\tau)$ are discontinuous at $f_s \tau = -\frac{N}{2}, \dots, \frac{N}{2}$. Therefore, the critical time of a glitch occurrence is when the delay becomes an integer multiple of the sampling time T_s .

We estimate the impact of such an event in TDI under the worst-case assumption that the critical condition is met in the final delay operation when calculating the intermediary variable σ_{ij} (see (8)). In this case the glitch is additive in the final Michelson combination without the usual TDI transfer function applied that would suppress power at low frequencies. We use (34) to estimate the contribution to the PSD of the discontinuity in the first derivative ($\hat{q} = 1$) of the kernel function.

In figure 5 we plot the result of this computation as the solid blue line. To distinguish spectral leakage and its origin we also consider the case without leakage (light blue) treating the spectral window like a Dirac-delta function[¶]. This provides us with a scaled version of $|\Delta \tilde{h}_q(f)|^2 \cdot S_x(f)$ and, therefore, with a sense for the origin of the leaked power. We note that for LISA in-band frequencies the leaked contribution from out-of-band frequencies, i.e. 1 Hz to 2 Hz, dominates. Thus, suppressing laser frequency noise close to the Nyquist rate using a low-pass filter applied prior to TDI would greatly reduce the impact of the interpolation glitch for the specific case of Lagrange interpolation. Note that such an additional filter would require a large number of coefficients to realize a sharp transition at 1 Hz (i.e. a close-to-unity response in the LISA band and appropriate suppression between 1 Hz and 2 Hz). This comes with a few drawbacks, e.g., the size of data gaps is increased and the introduction of an additional group delay.

[¶] Note, that we cannot design the window function $w(\tau)$ such that we achieve this behaviour. Thus, this is rather a hypothetical scenario used for illustrative purposes.

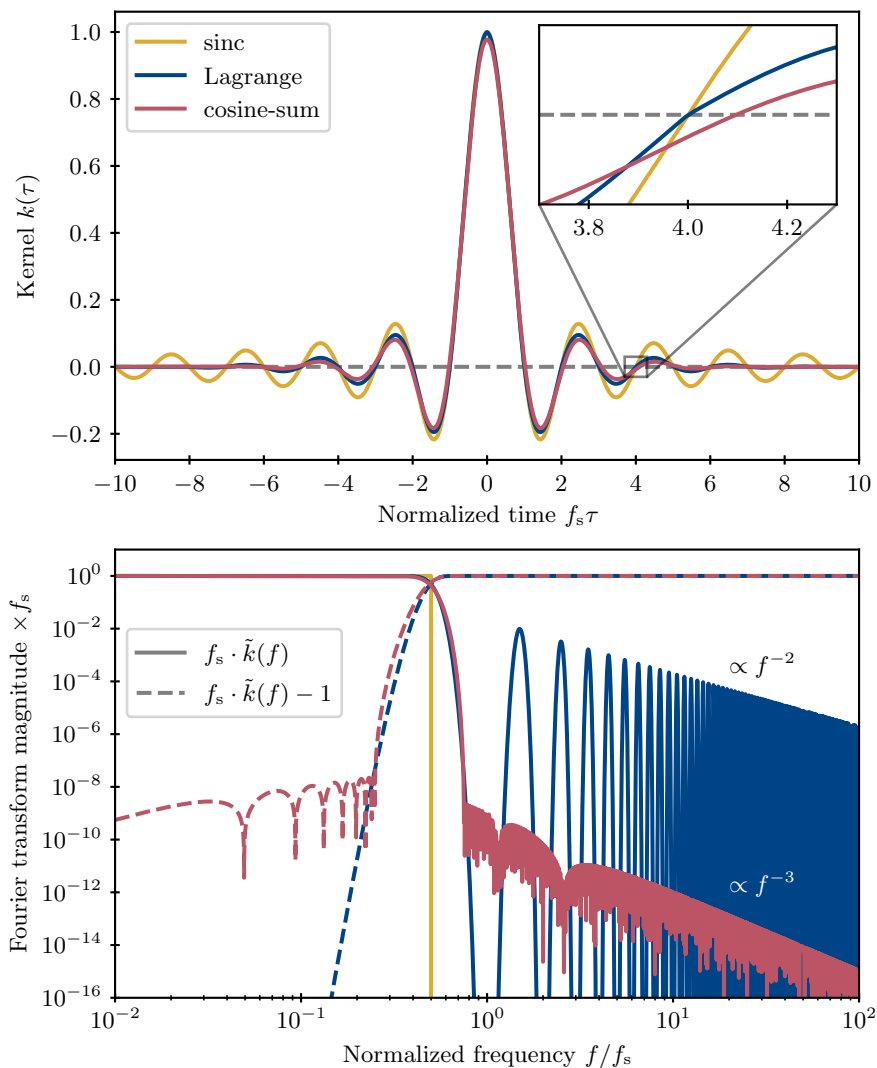


Figure 6. Comparison of the ideal sinc-kernel in yellow, the order 41 Lagrange kernel ($N = 42$) in blue and the cosine-sum kernel ($N = 22$) in red. The upper panel presents the time-domain kernel functions and their different behaviours at integer times (highlighted in the zoomed-in insert). Both the sinc-kernel and Lagrange kernel are not displayed completely as they reach past the x-axis' limits. The lower panel shows the normalized Fourier transform in solid and its difference from unity in dashed.

5. Cosine-sum Kernel

The short-comings of Lagrange interpolation call for an alternative interpolation method. In this section, we propose a novel interpolation kernel which allows us to reduce the width of $k(\tau)$ (and therefore a reduction of interpolation coefficients) and, simultaneously, suppress the impact of discontinuities in the interpolation kernel in TDI. To tackle these aims, we explore kernel functions that are derived from a finite Fourier series that only consider the even cosine contributions. For this reason, we dub this

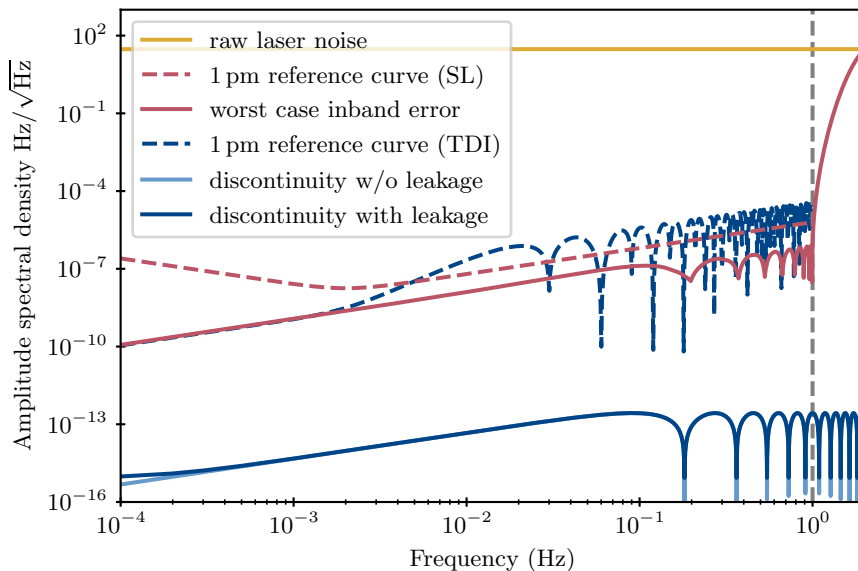


Figure 7. ASDs of interpolation errors for the cosine-sum kernel with otherwise identical parameters as figure 5. For this choice of kernel both the worst-case in-band interpolation error (red) and the ASD estimate of the leading order discontinuity (blue), i.e. in the second derivative ($\hat{q} = 2$), stay below their respective 1 pm reference curve (in dashed). The modeled ASD estimates of the discontinuity with and without leakage are almost identical, indicating that additional in-band power is not leakage-dominated.

novel family of kernels “cosine-sum kernels”. They are defined as

$$k(t) = \text{rect}\left(\frac{t}{NT_s}\right) \sum_{n=0}^{N-1} a_n \cdot \cos\left(2\pi f_s \frac{n}{N} t\right), \quad (39)$$

where NT_s is the width of the kernel (and therefore N the number of coefficients drawn from it) and a_n the Fourier coefficients.

This formulation of the kernel function is highly versatile and in order to fulfil the constraints of the kernel design the coefficients a_n have to be determined. For an effective kernel design for the constant delay operation we require two conditions which we derive from (22). Firstly, the in-band response (0 Hz to 1 Hz) of the (normalized) Fourier transform $f_s \cdot \tilde{k}(f)$ should be close to unity and, secondly, the out-of-band response ($f \geq 3$ Hz) should be well attenuated to suppress the aliased contributions in (22). Those conditions are cast into a minimax optimization problem that can be solved iteratively using a variant of the Parks-McClellan algorithm [18]. By defining appropriate weights for the error function we are able to design a kernel function that accounts for the f -slope of the 1 pm reference curve (in frequency units). The result is presented in Appendix A and the accompanying figure therein.

As derived in section 3 we require a sufficiently smooth kernel function to avoid the introduction of glitch-like features in the data. The family of cosine-sum kernels in (39) is infinitely differentiable almost everywhere except at the boundaries $\tau = \pm NT_s/2$

where even derivatives are discontinuous. To control the effect of those discontinuities (see (34)) we also include the possibility to increase the smoothness of $k(\tau)$ by imposing additional conditions on the a_n such that $k^{(2q)}(\tau) = 0$ with $q \geq 0$ at the boundaries. This comes at the cost of degrading the ideal response of $\tilde{k}(f)$ as some degrees of freedom have to be invested in fulfilling those boundary conditions. This is discussed in more detail in Appendix A.

Our final proposal uses $N = 22$ coefficients and assures continuity in the first derivative (one additional degree of smoothness compared to the Lagrange kernel). The resulting kernel function $k(\tau)$ and its Fourier transform are presented in figure 6. The kernel functions for Lagrange interpolation (blue) and of the cosine-sum family (red) are almost identical. However, on closer inspection there are some notable differences highlighted by the zoomed-in insert. First, opposed to the ideal sinc-function and the Lagrange kernel the cosine-sum kernel is non-unity at $\tau = 0$ and is lacking zero crossings at $f_s\tau \in \mathbb{Z}$ (with relative differences of up to a few percent). As a result, the cosine-kernel does not strictly constitute an interpolator as the interpolating function in (10) does not cross the original samples⁺. Furthermore, the cosine-sum kernel appears smooth over the entire domain (except the boundaries) as discussed already before.

Finally, let us investigate the in-band performance of the cosine-sum kernel for constant and time-varying delays. Analogously to the previous section, in figure 7, we present the worst-case interpolation error (red) and the ASD estimate of the discontinuity (blue) in the second derivative ($\hat{q} = 2$). Both stay below their 1pm reference curve (single-link and TDI-adjusted [9], respectively). We also note that the ASD estimates for the discontinuity are not leakage-dominated as $\Delta\tilde{h}_{\hat{q}}(f)$ is not peaked at high frequencies as it is the case for the Lagrange kernel, so prior filtering of the raw measurements is not required.

6. Numerical Simulations

In the following, we demonstrate the impact of the choice of interpolation kernel in TDI for a realistic LISA setup. Therefore, we run numerical simulations using LISA Instrument [19]. We simulate interferometric data at 4 Hz for 10 000 s to resolve down to the band limit of 10^{-4} Hz only including white laser frequency noise at a level of $30 \text{ Hz}/\sqrt{\text{Hz}}$. Furthermore, to simplify the setup we assume a single laser per spacecraft to directly yield the η variable (see (1)) as an output of the simulation. For realistic time-varying delays we choose numerical orbit files provided by ESA [4] and pick the starting time of the simulation such that the round-trip delays d_{12131} and d_{13121} become exactly integer delays in the centre of the domain. When calculating the second-generation Michelson variable \dot{X}_2^* as defined in (9) using PyTDI [21] the interpolation glitch for

⁺ In other words, applying the delay operation with $d = 0$ does not yield the original time series.

^{*} As LISA Instrument simulates interferometric data in units of frequency the expressions in (9) need to be adjusted by replacing each delay operator by its Doppler shift corrected equivalent [20]. The result of this calculation is the Michelson combination in units of frequency indicated by the dot.

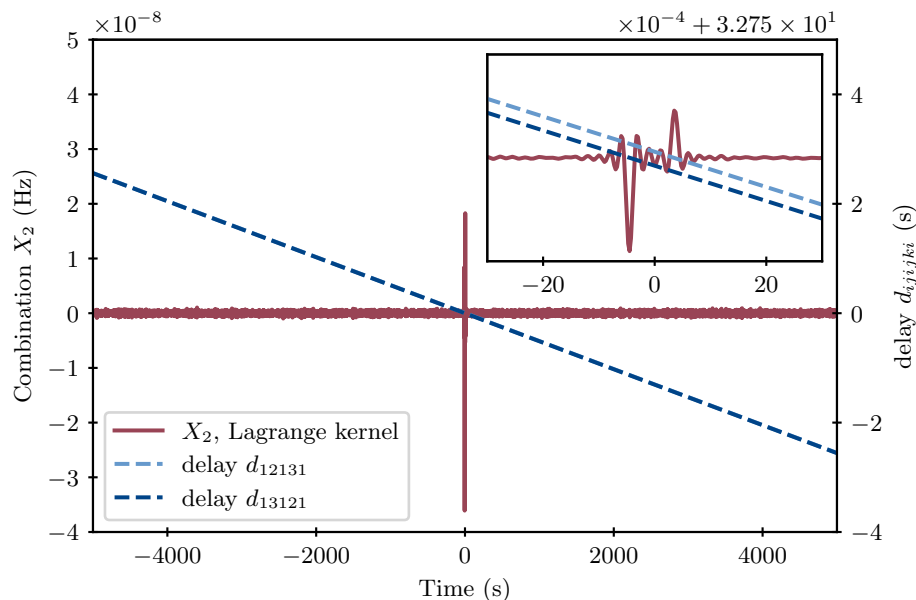


Figure 8. Second-generation Michelson combination X_2 computed using Lagrange interpolation (order 41). In dark red the low-pass filtered time series is shown exhibiting a prominent glitch at the centre. The dashed lines represent the round-trip delays d_{12131} (light blue) and d_{13121} (dark blue) which are almost identical. The inset shows a zoomed-in view which reveals that the time series of X_2 contains two distinct features that happen when each of the round-trip delays crosses the numerical value 32.75 s (an integer multiple of the sampling time $T_s = 0.25$ s).

the kernel functions discussed in the previous section enters through the calculation of the intermediary variable σ . This presents the worst case coupling, as the effect of the glitch is not attenuated by the transfer function of TDI that usually acts like a time derivative, thus suppressing low-frequency components.

In figure 8 we show the time-domain representation of the Michelson variable X_2 (in red) using Lagrange interpolation. After applying a low-pass filter to suppress the dominant contributions to the interpolation error at high frequencies the interpolation glitch becomes clearly visible in the centre of the domain when the round-trip delays d_{12131} (dashed light blue) and d_{13121} (dashed dark blue) are equal to 32.75 s which is an integer multiple of the sampling time of 0.25 s. When zooming in on the glitch it separates into two distinct features which can be unambiguously attributed to the integer-delay crossing of each of the round-trip delays.

To circumvent this strong interpolation glitch we compute the same TDI variable using the cosine-sum kernel introduced in section 5. As it disappears in the time-domain result we resort to the spectral representation to check for anomalies. In figure 9 we plot the periodograms (using the same Kaiser window as before with $\beta = 30$) of the Michelson variables computed using the cosine-sum kernel (blue) and Lagrange interpolation (dark red). As expected, the cosine-sum kernel performs closer to the 1 pm reference curve [9] than Lagrange interpolation for most of the band. However, the latter contains extra

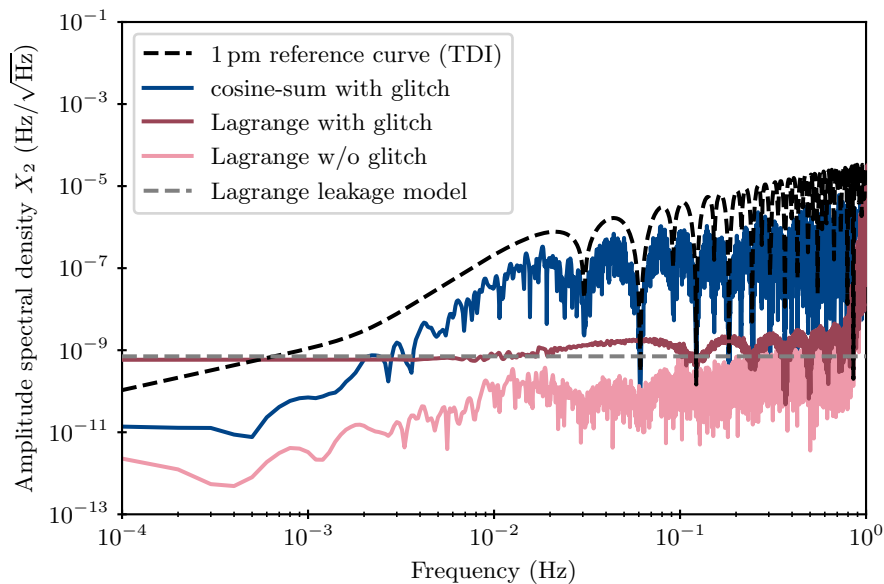


Figure 9. ASD of second-generation Michelson combination X_2 for different interpolation schemes. Periodograms of 10 000 s-datasets including the critical time (c.f. figure 8) are shown for numerical TDI calculations using the cosine-sum kernel (dark blue) and Lagrange interpolation (dark red). In light red we plot the result for Lagrange interpolation for a time slice of the data that excludes the glitch. For reference, we plot the level of additional leakage at DC due to an interpolation glitch in dashed grey and the 1 pm reference curve (propagated through TDI [9]) in dashed black.

power that is not explained by the usual (constant delay) in-band interpolation error. We confirm this by repeating the experiment using Lagrange interpolation for data shifted to a slightly later time to exclude the glitch (light red). The level of the extra power in the experiment including the glitch (dark red) is consistent with the model (grey) derived in section 4 assuming \dot{d} has a magnitude of approximately 5×10^{-8} . We calculate the level of spectral leakage at DC due to an interpolation glitch using (34) assuming $S_x(f) \rightarrow S_{\dot{p}}(f) = 4 \sin^2(4\pi fL) \cdot (30 \text{ Hz}/\sqrt{\text{Hz}})^2$ with $L = 8.19$ s. The oscillatory features visible at higher frequencies can be explained by the fact that the pair of interpolation glitches enter with a separation of approximately 10 s which explains the nulls at multiples of 0.1 Hz.

7. Conclusion

Interpolation is an integral function of TDI which is needed to suppress laser frequency noise in LISA. TDI forms equal-arm interferometers by building linear combinations of time-shifted beatnote phases of heterodyne interferometers. The time-shift operation requires an extremely accurate interpolation method to cancel out laser phases and suppress laser frequency noise by up to nine orders of magnitude. In the past, Lagrange interpolation was used [13] for this task. However, we found that it produces glitch-like

features occurring when time-varying delays become integer multiples of the sampling time.

In this paper we develop a generalized framework to describe interpolation errors arising when time-shifting discrete-time data samples. We limit ourselves to interpolation methods that are defined as a convolution of a kernel function with the data to yield a continuous representation. For any given constant delay, the in-band interpolation error can be directly calculated from the kernel function. In case of a time-varying delay, the delay operation becomes time-variant and, thus, cannot be represented as a linear time-invariant system any more. The consequence is spectral leakage, which is contaminating the LISA band with excess power. The level of spectral leakage is dependent on the rate of change of the delay and the degree of smoothness of the kernel function.

Lagrange interpolation has been the standard interpolation method for TDI since its inception. Previous investigations of interpolation method performance only considered constant time delays [13]. In this paper, we demonstrate that Lagrange interpolation for a realistic LISA configuration is insufficient as the effect of spectral leakage rises above the 1 pm reference curve at low frequencies. Here, we assume a delay derivative of the order of 10^{-7} , which is a typical value for the round-trip delay in the Michelson combination (d_{12131} and d_{13121}), and choose an observation time of 10 000 s to resolve down to the low-end of the LISA band. The reason for the high level of spectral leakage is the discontinuity of the Lagrange kernel function in its first derivative.

As a solution, we propose a new family of versatile kernel functions composed of a sum of cosine functions (see (39)). We describe a method to efficiently optimize the free parameters of the cosine-sum kernel to yield a sufficient in-band performance and a high degree of smoothness. At the same time, we aim to minimize the width of the kernel (which translates directly into the number of interpolation coefficients) to reduce the cost of the delay operation and be more resilient to boundary effects. We find that a cosine-sum kernel that possesses a continuous first derivative and yields 22 interpolation coefficients suffices to achieve adequate in-band interpolation errors and suppress additional spectral leakage. This constitutes a reduction in number of interpolation coefficients by roughly a factor of two. For reference, we print the 22 coefficients that define the optimized cosine-sum kernel in table A1.

To numerically check the performance of both interpolation kernels we run LISA simulations assuming realistic dynamics based on orbit files provided by ESA. We intentionally choose a time frame of the mission where the round-trip delays d_{12131} and d_{13121} become integer multiples of the sampling time of the data. This results in a prominent glitch in the time-domain when calculating the second-generation Michelson variables in their factorized form, which in turn leads to strong spectral leakage. We then evaluate the periodogram for the TDI variable X_2 obtained using both kernels, the Lagrange and the optimized cosine-sum kernel. The ASD estimate of the former is affected by spectral leakage that is consistent with the levels predicted by the derived model. On the contrary, the periodogram of X_2 evaluated using the cosine-sum kernel

is free of excess power.

We therefore suggest using the cosine-sum kernel instead of Lagrange interpolation for the time-shift operation in TDI. This choice drastically cuts down the number of interpolation coefficients, and thus the computational cost, by a factor of two and reduces the amount of invalid samples at the edges of the time series or around gaps where the interpolation kernel does not overlap completely with the data. Moreover, the cosine-sum kernel suppresses additional spectral leakage induced by discontinuities in the kernel function to adequate levels.

Acknowledgments

The authors thank the LISA Simulation Working Group and the LISA Simulation Expert Group for the lively discussions on all simulation-related activities. M.S., A.H., M.L. and P.W. gratefully acknowledge support by the Centre National d'Études Spatiales (CNES). M.S. is supported by the research program of the Netherlands Organisation for Scientific Research (NWO). J-B.B. and G.W. acknowledge the support of the UK Space Agency, UKSA, through grant ST/Y004906/1. O.H. acknowledges the support of the German Space Agency, DLR. The work is supported by the Federal Ministry for Economic Affairs and Climate Action based on a decision by the German Bundestag (FKZ 500Q1801 and FKZ 500Q2301).

Appendix A. Optimizing the Cosine-sum Kernel

Using the class of cosine-sum kernels introduced in section 5 we can optimize the frequency response of the interpolation kernel. This is achieved by choosing a set of coefficients $\{a_n\}_{n=0}^{N-1}$ that fulfil some optimality criteria. For the interpolation method in TDI, we identify two such criteria in section 3; the in-band performance of interpolation and the smoothness of the kernel. In (22) we relate the Fourier transform of the kernel to the worst-case interpolation error over all possible values of the delay d . This formula tells us that $\tilde{k}(f)$ should be unity inside the band and vanishing for frequencies $|f| > \frac{f_s}{2}$.

Therefore, in the first step, we shall derive the Fourier transform of the cosine-sum kernel defined in (39). A similar derivation is given in [22]. We start by expressing the Fourier transform as

$$\tilde{k}(f) = \frac{NT_s}{2} \sum_{n=0}^{N-1} a_n (\text{sinc}(NT_s f + n) + \text{sinc}(NT_s f - n)), \quad (\text{A.1})$$

since the cosine transforms to a pair of Dirac-delta functions which shift the argument of the sinc-function (which is the Fourier transform of the rectangular function). Next, we introduce the normalized frequency $\xi = NT_s f$ for the sake of brevity and rewrite the

sinc-function as $\text{sinc}(\xi \pm n) = \frac{(-1)^n \text{sinc}(\pi\xi)}{\xi \pm n}$. We arrive at the simplified expression

$$\tilde{k}(\xi) = NT_s \text{sinc}(\xi) \sum_{n=0}^{N-1} a_n (-1)^n \frac{\xi^2}{\xi^2 - n^2}, \quad (\text{A.2})$$

$$= \underbrace{\frac{\text{sinc}(\xi)}{\prod_{n=1}^{N-1} \xi^2 - n^2}}_{\equiv R(\xi)} \cdot P(\xi^2), \quad (\text{A.3})$$

which can be recast into a product of the function $R(\xi)$ defined above and a polynomial $P(x)$ in ξ^2 of degree $N - 1$. This is achieved by contracting the sum of fractions in the first line into a single fraction with a common denominator. The polynomial also absorbs the free parameters a_n . Therefore, the optimization problem can be restated as finding the polynomial $P(x)$ such that aforementioned conditions are fulfilled. To relate back to the parameters a_n required to compute (39) we notice the following relationship. Let us evaluate the Fourier transform of the kernel at $\xi = m = 0, 1, \dots, N - 1$. Comparing the results from equations A.1 and A.3 we find

$$a_m = \frac{(-1)^m}{NT_s} \cdot \frac{P(m^2)}{\prod_{\substack{n=0 \\ n \neq m}}^{N-1} m^2 - n^2}, \quad (\text{A.4})$$

making use of l'Hôpital's rule for calculating the limit of $R(\xi)$ for $\xi \rightarrow m$ in (A.3).

Let us now turn back to the original optimization problem; finding the set of coefficients $\{a_n\}_{n=0}^{N-1}$ defining the cosine-sum kernel that fulfil the aforementioned optimality criteria. We define the weighted error function as

$$E(\xi) = W(\xi) \left(\tilde{k}(\xi) - D(\xi) \right), \quad (\text{A.5})$$

where $W(\xi)$ denotes frequency dependent weights and $D(\xi)$ the desired response which is unity for frequencies until the pass-band frequency f_{pass} and zero from the stop-band frequency f_{stop} . To obtain the coefficients that respect the inband performance we have to minimize the maximum absolute weighted error over all normalized frequencies $\xi \in U = [0, NT_s f_{\text{pass}}] \cup [NT_s f_{\text{stop}}, \infty)$

$$\{a_n\}_{n=0}^{N-1} = \arg \min \max_{\xi \in U} |E(\xi)|. \quad (\text{A.6})$$

The solution to this problem is in general difficult to find. However, in our case we can recast the expression in (A.5) into

$$E(\xi) = \underbrace{W(\xi) \cdot R(\xi)}_{\hat{W}(\xi)} \left(P(\xi^2) - \underbrace{\frac{D(\xi)}{R(\xi)}}_{\hat{D}(\xi)} \right), \quad (\text{A.7})$$

by plugging in (A.3) which turns (A.6) into a weighted Chebyshev approximation problem as in [18]. We identify the corresponding weighting function $\hat{W}(\xi)$ and desired

response $\hat{D}(\xi)$. Furthermore, we require that the approximation is exact at DC, i.e., $E(0) = 0$. Additionally, in the numerical implementation of the algorithm, we simplify the weighting function as

$$\hat{W}(\xi) \sim \begin{cases} W(\xi) \cdot R(\xi) & \text{if } \xi \leq N - \frac{1}{2}, \\ \frac{(-1)^{N-1}}{\pi\xi} \frac{1}{\prod_{n=1}^{N-1} \xi^2 - n^2} & \text{else,} \end{cases} \quad (\text{A.8})$$

to omit the oscillations (and zero-crossings) from the sinc-function that cause numerical difficulties. The approximation is exact for $\xi \leq N - \frac{1}{2}$ and else the absolute value presents an upper bound for $|\hat{W}(\xi)|$. Therefore, it still respects at least the weighting implied by $\hat{W}(\xi)$. Furthermore, we use an equivalent expression for $R(\xi)$ in (A.8) to avoid numerical problems close to integer values given as

$$R(\xi) = \frac{1}{2} \frac{\sum_{n=0}^{N-1} \text{sinc}(\xi + n) + \text{sinc}(\xi - n)}{\sum_{n=0}^{N-1} (-1)^n \left(\prod_{\substack{m=0 \\ m \neq n}}^{N-1} \xi^2 - m^2 \right)}. \quad (\text{A.9})$$

Reducing the polynomial degree M of $P(x)$ improves the decay of $\tilde{k}(f)$ for $f \rightarrow \infty$ (which is equivalent to $\xi \rightarrow \infty$). Let us set $M = N - L$ where L is a positive integer between 1 and N . As we apply the limit to (A.3) we find that the Fourier transform decays as $f^{-(2L-1)}$. The case $L = 1$ yields the slowest decay but allows for many degrees of freedom to shape $\tilde{k}(f)$. On the contrary, $L = N$ results in $P(x)$ being a constant (only a single polynomial coefficient to tune) but a fast decay proportional to $f^{-(2N-1)}$. The decay of the Fourier transform is directly linked to the smoothness of the function. A function possesses continuous derivatives up to degree q if its Fourier transform decays at least as $f^{-(q+2)}$.

In figure A1 we illustrate the result of the optimization procedure using parameters that respect the LISA requirements. We assume a sampling frequency of $f_s = 4$ Hz and an upper band edge of 1 Hz which determines $f_{\text{pass}}/f_s = 1/4$ and $f_{\text{stop}}/f_s = 3/4$. The stop-band frequency follows from arguments of aliasing as the band $[0.5, 0.75]$ is aliased to $[0.25, 0.5]$ which is out-of-band. For sufficient in-band and out-of-band suppression we choose a minimum kernel width of $N = 22$. To obtain continuity in the first derivative of the kernel (decay of f^{-3}) we set $L = 2$. The weighting function $W(f)$ is defined as

$$W(f) = \begin{cases} (f + f_{\min})^{-1} & \text{if } 0 \leq f \leq f_{\text{pass}}, \\ 10 \cdot f_{\text{pass}}^{-1} \cdot (f/f_{\text{stop}})^3 & \text{else,} \end{cases} \quad (\text{A.10})$$

where f_{\min} is set to 0.25×10^{-4} and saturates the weighting function at low frequencies.

Consequently, the maximum error $\delta/W(f)$ (where $\delta = \max_{\xi \in U} |E(\xi)|$) shown in dashed black in figure A1 is proportional to the Fourier frequency in band which is desired to respect the LISA requirement curve, which exhibits the same frequency dependency. The weighting function of the interval $[f_{\text{stop}}, f_s]$ is set such that $\tilde{k}(f)$ follows the general decay of f^{-3} and is at least ten times smaller at f_{pass} than its

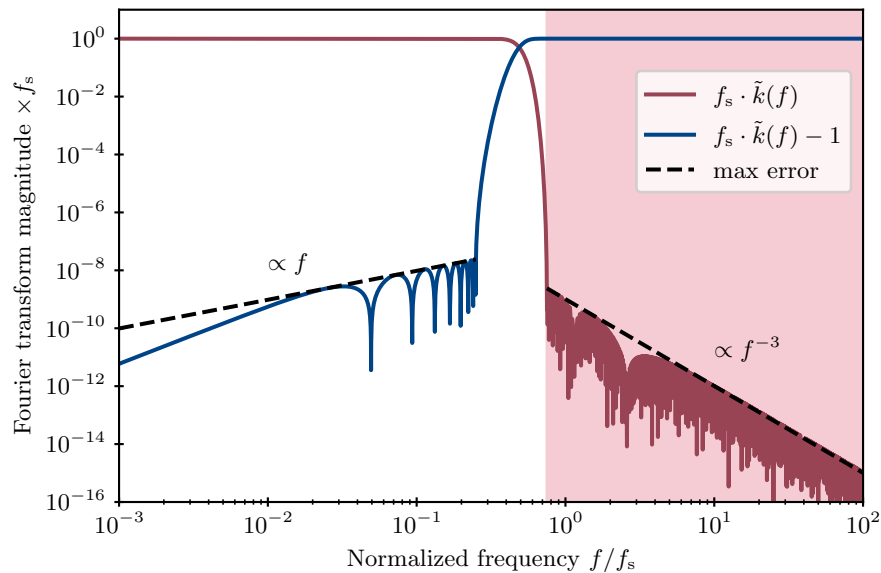


Figure A1. Result of optimization procedure for $N = 22$ and $L = 2$. The blue shaded region indicates the pass-band (from 0 to 0.75) and the red shaded region (from 0.75 to ∞) the stop-band. In dark red the Fourier transform of the kernel is plotted and in dark blue its difference from unity, which represent the (unweighted) error function in the stop-band and pass-band, respectively. In dashed black, we indicate the maximum error resulting from the specific choice of weighting function $W(f)$.

difference from unity at f_{pass} . The latter assures that after "aliasing" (see (22)) the performance is mostly limited by the in-band error of the kernel function. For reference the 22 coefficients are printed in table A1.

Coefficient	Value
a_0	$4.545\,454\,545\,454\,545\,6 \times 10^{-2}$
a_1	$9.090\,909\,080\,555\,947\,8 \times 10^{-2}$
a_2	$9.090\,909\,105\,336\,986\,2 \times 10^{-2}$
a_3	$9.090\,909\,130\,168\,918\,5 \times 10^{-2}$
a_4	$9.090\,908\,933\,518\,747\,3 \times 10^{-2}$
a_5	$9.090\,908\,948\,615\,096\,5 \times 10^{-2}$
a_6	$9.090\,806\,325\,825\,737\,1 \times 10^{-2}$
a_7	$9.080\,977\,692\,383\,675\,2 \times 10^{-2}$
a_8	$8.947\,443\,767\,375\,878\,9 \times 10^{-2}$
a_9	$8.260\,933\,048\,802\,579\,5 \times 10^{-2}$
a_{10}	$6.482\,160\,624\,671\,153\,0 \times 10^{-2}$
a_{11}	$3.866\,785\,366\,597\,749\,7 \times 10^{-2}$
a_{12}	$1.582\,165\,244\,645\,712\,0 \times 10^{-2}$
a_{13}	$3.986\,379\,129\,878\,200\,2 \times 10^{-3}$
a_{14}	$5.288\,158\,910\,630\,947\,0 \times 10^{-4}$
a_{15}	$2.687\,121\,911\,766\,724\,9 \times 10^{-5}$
a_{16}	$1.819\,290\,936\,243\,840\,4 \times 10^{-7}$
a_{17}	$4.277\,561\,257\,235\,863\,6 \times 10^{-11}$
a_{18}	$6.425\,048\,367\,000\,382\,3 \times 10^{-11}$
a_{19}	$1.273\,480\,487\,008\,691\,4 \times 10^{-10}$
a_{20}	$-1.095\,346\,160\,075\,071\,3 \times 10^{-10}$
a_{21}	$5.279\,955\,283\,504\,458\,7 \times 10^{-11}$

Table A1. Optimized coefficients a_n of the cosine-sum kernel defined in (39).

References

- [1] Colpi M *et al.* 2024 LISA Definition Study Report (*Preprint* 2402.07571)
- [2] Amaro-Seoane P *et al.* (LISA) 2017 Laser Interferometer Space Antenna (*Preprint* 1702.00786)
- [3] Seoane P A *et al.* (LISA) 2023 *Living Rev. Rel.* **26** 2 (*Preprint* 2203.06016)
- [4] Martens W and Joffre E 2021 *J. Astronaut. Sci.* **68** 402–443
- [5] Vallisneri M 2005 *Phys. Rev. D* **72** 042003 [Erratum: *Phys.Rev.D* 76, 109903 (2007)] (*Preprint* gr-qc/0504145)
- [6] Tinto M and Dhurandhar S V 2021 *Living Rev. Rel.* **24** 1
- [7] Shaddock D A, Tinto M, Estabrook F B and Armstrong J W 2003 *Phys. Rev. D* **68** 061303 (*Preprint* gr-qc/0307080)
- [8] Cornish N J and Hellings R W 2003 *Class. Quant. Grav.* **20** 4851–4860 (*Preprint* gr-qc/0306096)
- [9] Staab M, Lilley M, Bayle J B and Hartwig O 2024 *Phys. Rev. D* **109** 043040 (*Preprint* 2306.11774)
- [10] Bayle J B, Lilley M, Petiteau A and Halloin H 2019 *Phys. Rev. D* **99** 084023 (*Preprint* 1811.01575)
- [11] Staab M 2023 *Time-delay interferometric ranging for LISA* Ph.D. thesis Leibniz U., Hannover
- [12] Reinhardt J N, Staab M, Yamamoto K, Bayle J B, Hees A, Hartwig O, Wiesner K, Shah S and Heinzel G 2024 *Phys. Rev. D* **109** 022004 (*Preprint* 2307.05204)
- [13] Shaddock D A, Ware B, Spero R E and Vallisneri M 2004 *Phys. Rev. D* **70** 081101 (*Preprint* gr-qc/0406106)

- [14] Halloin H 2018 Note on decimation and interpolation filters for LISA simulation Tech. Rep. LISA-APC-INST-TN-003 APC
- [15] Jenkins G M and Watts D G 1968 *Spectral analysis and its applications* Holden-Day series in time series analysis (San Francisco: Holden-Day) ISBN 978-0-8162-4464-5
- [16] Tinto M, Estabrook F B and Armstrong J W 2004 *Phys. Rev. D* **69** 082001 (*Preprint* gr-qc/0310017)
- [17] Nuttall A 1981 *IEEE Transactions on Acoustics, Speech, and Signal Processing* **29** 84–91
- [18] Parks T and McClellan J 1972 *IEEE Transactions on Circuit Theory* **19** 189–194
- [19] Bayle J B, Hartwig O and Staab M 2024 Lisa instrument URL <https://doi.org/10.5281/zenodo.13809621>
- [20] Bayle J B, Hartwig O and Staab M 2021 *Phys. Rev. D* **104** 023006 (*Preprint* 2103.06976)
- [21] Staab M, Bayle J B and Hartwig O 2023 Pytdi URL <https://doi.org/10.5281/zenodo.8429119>
- [22] Albrecht H H 2010 *The Open Signal Processing Journal* **3** 20–29 ISSN 18768253 URL <http://benthamopen.com/ABSTRACT/TOSIGPJ-3-20>